https://doi.org/10.1016/j.clay.2021.106326

**Title:** Geopolymer-hydrotalcite hybrid beads by ionotropic gelation

**Authors:** Elettra Papa[a], Annalisa Natali Murri[a], Angelo Vaccari[a,b], Elena Landi[a], Valentina Medri[a]*

[a] National Research Council of Italy, Institute of Science and Technology for Ceramics (CNR-ISTEC), Via Granarolo 64, 48018 Faenza, RA, Italy

[b] "Toso Montanari" Department of Industrial Chemistry, University of Bologna, Viale Risorgimento 4, 40136 Bologna, Italy

*Corresponding author e-mail: valentina.medri@istec.cnr.it

**Abstract:**

Geopolymer beads are already known as alternative, cost-effective, environmentally friendly adsorbents for cationic species in wastewater treatment. To broaden the spectrum of applications it is necessary to functionalize the geopolymer matrix with fillers and create composites.

In this study, being hydrotalcite an anionic exchanger, highly reproducible geopolymer-hydrotalcite hybrid beads were synthesised. Starting from a metakaolin-based geopolymer slurry added with a sodium alginate solution and hydrotalcite powder as filler, millimeter-sized beads were shaped by ionotropic gelation using injection-solidification in $CaCl_2$ solution. In order to vary the porosity and related properties of the beads, two consolidation methods were adopted: a conventional consolidation in a heater set at 60°C and a freeze-drying process. Beads differed in terms of dimension and morphology with an open porosity ranging from 50 to 70% and specific surface area from 12 to 23 $m^2 g^{-1}$. Mechanical resistance, following ISO 18591, was about 6 MPa making the beads easy to handle and resistant in the recovery, separation and filtration operations of aqueous systems.

**Keywords:** Geopolymer; Hydrotalcite; Ionotropic gelation; Freeze-drying; Porosity; Mechanical testing

## Introduction:

Contamination of water bodies, as lakes, rivers and seas, is among the major issues concerning environmental pollution, due to the constant industrial growth worldwide. Different contaminants can be found in wastewater as bacteria, heavy metals, dyes, excessive presence of nutrients as nitrogen and phosphorous which induce eutrophication, and others (Tan et al., 2020).

Several techniques could be adopted for wastewater treatment to reduce the level of contaminants, and among them adsorption shows fewer limitations, and although may not be as effective compared to the other established methods, its simple protocol, easiness of design and cost effectiveness have made it a universal technique (Tan et al., 2020). Numerous efficient adsorbents are reported in literature, however they are often expensive and nonselective, such as commercial activated carbons (Crini et al., 2019), and they are difficult to shape. These limitations have increased the research towards lower cost but effective and environmentally friendly alternatives. In light of this, lately, geopolymers (i.e. a special class of alkali-activated materials) have been reported as alternative adsorbents, exhibiting good pollutant removal properties through adsorption processes (Lukkonen et al., 2019).

Geopolymer technology is gaining interest in research and development, because it is a versatile material with many potential applications in water and wastewater treatment (Lukkonen et al., 2019). These include adsorbents/ion-exchangers, membranes and filtration media, photocatalysts, solidification/stabilization, and other less used applications as antimicrobial materials, pH buffers and carrier media for bioreactors (Lukkonen et al., 2019; Asin et al., 2019; Siyala et al., 2018; Rasaki et al., 2019). In addition, the analogies with zeolites (Bortnovsky et al., 2008) and the ease of adding photoactive phases (Medri et al., 2020b), make geopolymers promising materials also for resistance to fouling during wastewater treatments.

Geopolymers are porous inorganic polymers with great eco-friendliness potential. They are obtained at low temperature (from room temperature up to 100°C) by a chemical reaction between an alumino-silicate source material (also power-plant by-products such as fly ashes) and a highly alkaline solution (Davidovits, 2008). The geopolymerization is a water-based reaction that leads, in general, to amorphous materials with good physical and chemical stability and a porous structure with high specific surface area. Furthermore, geopolymers possess ionic exchange and electrostatic interaction properties, thanks to the negatively charged surface of their final three-dimensional network, due to the presence of Al in tetrahedral coordination. Commonly, cations as sodium and potassium balance the geopolymer lattice, endowing the material with ionic exchange capacity, in analogy with zeolites, its crystalline counterpart (Bortnovsky et al., 2008).

Geopolymers are intrinsically mesoporous and the micro-meso-macro-ultramacro porosity of the material can be tailored by adding fillers (Papa et al., 2018) or using techniques able to induce porosity at different levels, as ice-templating or direct foaming (Papa et al., 2015; Medri et al., 2013). Therefore, the porous structure and the ionic exchange capacity make these materials interesting for applications in the field of adsorption. Several studies report the preferential adsorption of cations by these materials, as $NH_4^+$ (Lukkonen et al., 2016), heavy metals as nickel, zinc, copper, cadmium, lead, chromium, calcium, caesium, cobalt, magnesium, and arsenic (Siyala et al., 2018), and cationic dyes (Siyala et al., 2018; Papa et al., 2020).

Conversely, the adsorption of anionic species has been poorly investigated and often additives or modifications have been introduced to change the absorbent capacity of geopolymers. In this regard, a barium-modified blast furnace slag geopolymer was used for the removal of sulphates (Runtti et al., 2016), while geopolymers modified with $CeO_2$ and $Fe_2O_3$ have been tested for the removal of $F^-$ from wastewater (Wang et al., 2020; Chen et al., 2019). Moreover, attempts were made to generate hydrotalcite phases within the geopolymer matrix or add calcined hydrotalcites for the removal of $Cs^+$ and Se oxyanions (Tian et al., 2020; Tian et al., 2019). In fact, synthetic hydrotalcite, known as layered double hydroxides (LDH), was reported to be a good adsorbent for anionic species including

$B(OH)_4^-$, $AsO_3^{3-}$, $AsO_4^{3-}$, $SeO_3^{2-}$, $SeO_4^{2-}$, etc. (Costantino et al., 2017; Goh et al., 2008; Ji et al., 2017). LDH could be generally represented by the formula $[M^{2+}_{1-x}\ M^{3+}_{x}\ (OH)_2]^{x+}\ [A^{n-}]_{x/n} \cdot mH_2O$, where $M^{2+}$ and $M^{3+}$ are divalent and trivalent cations, coordinated octahedrally by hydroxyl groups to form two-dimensional positively charged layers. A represents the interlayer anion, with charge n, that balance the positively stacked layers, while x is the fraction of the trivalent cation and m the water of crystallization (Cavani et al.,1991; Vaccari, 1998).

Furthermore, the basic reason for designing adsorbents relies on the fact that fine or ultrafine inorganic particles are unusable in fixed beds or any flow-through system because of excessive pressure drops and poor mechanical strength (Pan et al., 2009). Moreover, they are difficult to recover and separate, especially during filtration of aqueous systems. For this purpose, geopolymer adsorbents were produced in the form of millimetre-sized beads using injection-solidification in different media such as polyethylene glycol (Tang et al., 2015; Ge et al., 2015; Novais et al., 2017), silicone oil (Liu et al., 2017; Tang et al., 2017), liquid nitrogen (Papa et al., 2019; Papa et al. 2020) and calcium chloride (Ge et al., 2017), the latter exploiting the ionotropic gelation of sodium alginate added to the geopolymer slurry (Medri et al., 2020a; Medri et al., 2020b). In details, ionotropic gelation process generally involves two basic steps: dispersion of a solution containing alginate into droplets and gelation to solidify the droplets. To produce the beads, a liquid-air dispersion method and an external gelation mechanism have been involved (Leong et al., 2016). The dripping method implies the extrusion, through a flat needle, of liquid geopolymer-alginate droplets into the air. At low volumetric flow rates, the liquid accumulated at the needle tip detaches as a discrete droplet once the gravitational force exceeds the surface tension. The drops fall into the gelling bath ($CaCl_2$) containing divalent cations, able to crosslink the alginate polymer chains and forming an “egg-box” structure (Leong et al., 2016). Because $CaCl_2$ salt is readily soluble in water, $Ca^{2+}$ ions in solution can instantaneously crosslink the alginate in the droplets, forming the beads. It must be pointed out that sodium alginate is a natural occurring polysaccharide biopolymer, a structural component of algal cell wall, widely used for biomolecule immobilization and a potent metal chelator (Mandal et al., 2012). Recently, the

use of biopolymers for adsorption has become more interesting thanks to their eco-friendly nature, inexpensiveness and abundance (Kumar et al., 2017). Moreover, studies have shown that supporting anionic clays, as hydrotalcites, on suitable support materials enhances their adsorption capacity because of dispersion of the clay particles on the surface of the support materials (Mandal et al., 2012; Mandal et al., 2008).

Therefore, the aim and the novelty of the present work are the developing for the first time of geopolymer spheres containing hydrotalcite as filler, where the use of alginate allows the production of highly reproducible, cost-effective and environmentally friendly composite beads, having both anionic and cationic exchange functions. The presence of porous and permeable alginate skeleton combined with the geopolymer matrix acts as a support allowing water to penetrate without washing out the trapped particles of hydrotalcite and increasing the mechanical performance of the adsorbents. The beads were obtained starting from a metakaolin-based geopolymer slurry added with a sodium alginate solution and a commercial hydrotalcite as filler. The beads were shaped by ionotropic gelation and finally consolidated adopting two processes, in order to vary and influence the porosity and related properties useful for adsorption purposes: a conventional consolidation in a heater set at 60°C and a freeze-drying process. The beads were then deeply characterized in terms of shape, dimensional distribution, morphology, microstructure, porosity, specific surface area and mechanical resistance.

## 2. Materials and Methods

### 2.1 Preparation of the starting slurries

The geopolymer slurry was prepared by mixing a potassium di-silicate solution ($H_2O$:$K_2O$=13.5, $SiO_2$:$K_2O$=2.0 molar ratio), prepared by dissolving KOH pellets (>85%, Sigma Aldrich) and fumed silica (99.8%, Sigma Aldrich) in deionized water under magnetic stirring, with metakaolin (Argical™ M1200S, Imerys, SSA= 25 $m^2$ $g^{-1}$, d50 =1.5 mm).

A homogeneous geopolymer slurry, with theoretical molar ratios $SiO_2$:$Al_2O_3$=4.0 and $K_2O$:$Al_2O_3$=0.8, was obtained by mixing the reagents with a planetary centrifugal mixer (THINKY MIXER ARE-500) set at 900 rpm.

The geopolymer slurry was blended with a 4 wt.% solution of sodium alginate (Aldrich) and mixed for 3 minutes at 900 rpm by the planetary centrifugal mixer for the subsequent spherification process (beads coded as GA).

The geopolymer-hydrotalcite composites were prepared adding to the geopolymer-alginate slurry a commercial Pural®70 hydrotalcite (coded HT), with Mg:Al molar ratio equal to 3.1, in different percentages (40 and 60 wt.% over the geopolymer dry weight; beads coded as GAHT40 and GAHT60, respectively).

For reference, an aqueous hydrotalcite slurry was prepared mixing deionized water, hydrotalcite and the sodium alginate solution (beads coded as HTA). The mixing ratio adopted for the formulation of the different slurries are reported in Table 1.

**2.2 Preparation of the beads by ionotropic gelation**

The beads were obtained exploiting the ionotropic gelation that occurs between sodium alginate and bivalent cations. The prepared slurries were dropped in a $CaCl_2 \cdot 2H_2O$ (Merck) solution (0.5 M) kept at 45°C under stirring, using a peristaltic pump equipped with a flat needle with an internal diameter of 1.36 mm. The beads, instantly shaped, were left in $CaCl_2$ solution for at least 30 min and then washed with hot water.

The beads were subjected to two different final consolidation processes: in one case beads were put in a heater at 60°C (beads coded with -H) to complete geopolymerization, while in the other case beads were put in a freeze dryer (Edwards Mod.MFD01, Crawley, UK), frozen at -40°C and then lyophilized (-40°C /+25°C, P= 8·10-2 torr). The lyophilized beads were then put in the heater at 60°C (beads coded with –L).

Ultimately, all the beads were rinsed in a deionized water bath for 24 h, to remove unreacted phases, and dried at 60°C.

A schematic diagram of the production process of the beads is reported in Fig. 1, while beads codes, percentage of hydrotalcite present in the consolidated beads and consolidation method are in listed in Table 1.

### 2.3 Characterization of the beads

Beads' morphological parameters were obtained analysing high-resolution images through the open access ImageJ program. For each different batch, 300 beads were observed, and the average major diameter together with their roundness (expressed by the program as 4 Area/($\pi$ * major axis$^2$)) were calculated for the "fresh" shaped beads (just removed from $CaCl_2$ solution) and after the two consolidation processes.

The microstructural features of the beads were examined by an Environmental Scanning Electron Microscope (E-SEM FEI Quanta 200). The samples were previously made conductive by applying a thin gold layer using a turbo-pumped sputter coater (Quorum Q150T ES).

The tapped density of the beads was obtained as the ratio of the mass of the beads to the volume occupied by them after tapping a graduated measuring cylinder.

Beads' pore size distribution, in the range of 0.0058–100 μm, was analysed by mercury intrusion porosimetry, MIP (Thermo Finnigan Pascal 140 and Thermo Finnigan Pascal 240).

The measurement of the specific surface area (SSA) has been carried out on the beads in a Thermo Scientific™ Surfer instrument. The specific surface area was calculated by the Brunauer–Emmett–Teller (BET) method, by means of nitrogen adsorption at 77 K.

Mechanical tests were performed simultaneously on several beads, at room temperature and using a die-plunger test, according to the international standard ISO 18591. The test was carried out using a universal testing machine (Zwick Z050, loading cell class 05, GmbH, Ulm, Germany) and a cross-head speed of 1 mm min$^{-1}$. The beads were subjected to uniaxial compressive loading in a confining

steel die, under specified ISO conditions. The mechanical test was repeated 3 times for each beads type. The applied standard allowed to calculate the average compressive strength (Pc) and the density of the compressed beads (ρc), the latter calculated applying Eq.1:

$$\rho c = \frac{m}{V} = \frac{m}{\{A \cdot [h + (lf - l)]\}} \qquad (1)$$

where:

ρc = density of the die-pressed compact;

m = mass of the die-pressed compact;

V = volume of the die-pressed compact;

A = base area of the die-pressed compact;

h = height of the die-pressed compact;

lf = overall displacement of the piston;

l = displacement of the piston over time.

## 3. Results and Discussion

### 3.1 Morphology and microstructure of the beads

"Fresh" beads, just shaped in $CaCl_2$, and after the two consolidation methods, in the heater and in the freeze-dryer, were investigated by image analysis.

During the production of the beads an external gelation mechanism occurs, where $Ca^{2+}$ ions diffuse inward into the interstitial spaces between the alginate polymer chains to initiate their crosslinking. First, the crosslinking occurs on the outer surface of the droplet, resulting in the formation of a semi-solid layer encasing the droplet with a liquid core. The beads remain in immersion in the crosslinking bath allowing a further diffusion of the $Ca^{2+}$ ions, via a concentration gradient, that finally leads to the hardening of the droplet core, too. As a result, beads are formed with a denser Ca-alginate network on the external surface layer, that randomly entangles the composite geopolymer-hydrotalcite core. Both processes allow to obtain reproducible, uniform and spherical beads with a roundness value around 0.90 (Table 2).

206 The average major diameter (Ø) and the diameter shrinkage after consolidation are reported in Table
207 2, while the major Ø distributions, for the different types of beads, are reported in Fig. 2.
208 In general, the fresh beads show an average diameter around 4 mm, which changes considerably
209 depending on the consolidation process. Indeed, beads undergo a substantial shrinkage after
210 consolidation in the heater, due to the removal of the residual trapped water between the alginate
211 chains. GA-H beads shrink by 35%, while the composite beads GAHT40-H and GAHT60-H reduce
212 their diameter by 26%. The reference sample HTA-H, having the highest water content, reduces the
213 average diameter by 40%.
214 The freeze-drying process allows to first freeze the water contained in the beads, which is
215 subsequently sublimated, avoiding the shrinkage of the beads due to water evaporation. In this case,
216 the shrinkage of sample GA-L, GAHT40-L and GAHT60-L is around 15%, while the reference HTA-
217 L reduces the diameter dimension only by 3%.
218 Based on the diameter distributions (Fig. 2) the consolidation in the heater allows to obtain a narrower
219 dimensional distribution of the beads, while the freeze-drying process slightly widens the size
220 distribution. However, the distributions highlight how the process enables to obtain highly
221 reproducible beads, which is of interest for a larger industrial scale production.
222 SEM images of beads (whole beads, cross section, external and internal surfaces), obtained from the
223 different slurries and subjected to the consolidation in the heater or in the freeze-dryer are showed in
224 Fig. 3 and Fig. 4, respectively.
225 Beads consolidated in the heater (Fig. 3) show a worm-like surface because of the higher formation
226 of Ca-alginate skeleton on the outer shell of the bead, directly in contact with the $CaCl_2$ solution. The
227 beads substantially shrink after drying, thus causing the Ca-alginate skeleton to fold and stack in the
228 characteristic worm-like shape (Medri et al., 2020a; Medri et al., 2020b) which is typical in the
229 production of alginate-based beads (Voo et al., 2016).
230 The GA-H internal microstructure is composed by a less distinguishable intermingled matrix of
231 geopolymer and alginate (Fig. 3c).

In general, the internal microstructure of the composite beads, GAHT40-H and GAHT60-H, evidences the presence of the hydrotalcite particles that are incorporated in the geopolymer-alginate mixed matrix (Fig. 3f,i). The hydrotalcite particles show a shell-like structure, which favors incorporation into the matrix (Papa et al., 2019) and their layered structure is well evident in the internal microstructure of the reference beads HTA-H (Fig. 3n). HTA-H beads appear as a set of hydrotalcite particles held together by the alginate, that acts as a glue (Fig. 3l), and the external surface results formed by rough and uneven bumps (Fig. 3m).

The freeze-drying process produces beads with a more porous structure (Fig. 4). The external surface of the freeze-dried beads appears compact, smooth and dense, while the internal microstructure is more porous, with filaments of alginate polymer. The internal presence of wire-like Ca-alginate and granular geopolymer forming a "honeycomb network" inner structure is due to the freeze-drying process as already observed by Ge et al. (Ge et al., 2017).

The macropores and the layer-by-layer structure, evident in the cross section of the beads (Fig. 4g,l), result from the removal of water between the crosslinked alginate polymer matrices during the freeze-drying process. Indeed, during the crosslinking process, water is expelled from the crosslinked polymer matrices into the inner core of the partially-gelled bead. Water remains thus trapped in between the forming thick Ca-alginate layers, because $Ca^{2+}$ ion solution continues to diffuse inward the bead, forming new layer of Ca-alginate and finally, as a consequence, the water-rich layer (Voo et al., 2016).

Also in this case, the composite beads GAHT40-L and GAHT60-L show the presence of hydrotalcite particles in the internal microstructure (Fig. 4f,i) and HTA-L beads result composed by hydrotalcite particles glued together (Fig. 4m).

### 3.2 Porosity and specific surface area

256 Tapped density, data obtained through MIP analysis and SSA values are reported in Table 3, while
257 pore size distributions of the different beads obtained after consolidation in the heater and in the
258 freeze-dryer are reported in Fig. 5 and Fig. 6 respectively.
259 The data are affected by the consolidation method used. The tapped density is equal to 0.5 g $cm^{-3}$ for
260 the beads obtained after consolidation in the heater and 0.4 g $cm^{-3}$ for the freeze-dried beads (Table
261 3). Freeze-dried beads show a bigger average diameter, occupying more volume in the cylinder, thus
262 lowering the tapped density.
263 The reference beads HTA-H and HTA-L show completely different values. HTA-H beads increase
264 the tapped density to 0.8 g $cm^{-3}$, because the decreased average beads diameter (Table 2) fixed the
265 weight. Conversely, HTA-L beads show the lowest tapped density value (0.2 g $cm^{-3}$) because, due to
266 the high-water content combined with the freeze-drying process, the beads are more porous, bigger
267 and lighter.
268 Regarding the MIP values, beads obtained after consolidation in the heater (-H) show an open
269 porosity and a total pore volume lower than the beads obtained after freeze-drying. Indeed, during
270 consolidation these beads shrink, compact and reduce their porosity. In general, the open porosity is
271 around 50% for all the beads, with the exception of HTA-H beads that, because of the highest
272 shrinkage (Table 2), reduce their open porosity to 20%.
273 Opposite behavior occurs for the freeze-dried beads (-L), where the sublimation of ice avoids the
274 shrinkage. They show higher porosity, comprised in the range of 60-70%, with HTA-L beads having
275 the highest open porosity value (73%) because of the high water content.
276 These different behaviors are visible also in the pores size distributions reported in Fig. 5 (-H beads)
277 and Fig. 6 (-L beads). Prevalently monomodal distributions are observed for beads obtained after
278 consolidation in the heater (Fig. 5), with the most frequent pore size diameter (modal pore Ø) centered
279 at 0.15 µm for GA-H and at slightly higher values, around 0.30 µm, for the composite beads
280 GAHT40-H and GAHT60-H (Table 3). Also, in this case, the exception is given by the HTA-H beads

281 that show a more enlarged pore size distribution (Fig. 5b) with the modal pore diameter centered at
282 lower value, 0.01 µm, because of the higher contraction of the beads.
283 The freeze-dried beads show broader distributions, with modal pore diameters centered around the
284 same values obtained for the beads consolidated in the heater (Table 3). HTA-L beads greatly
285 increased the modal pore size diameter compared to HTA-H beads, passing from 0.01 µm to 25.10
286 µm, thus showing a distribution located mostly in the macropores region.
287 As regard to the SSA values, GA-H beads have the highest value (23 $m^2 g^{-1}$), probably because they
288 are mainly composed by the geopolymer matrix and, in addition, consolidated in the heater, which
289 favors the geopolymerization reaction. The introduction of the hydrotalcite filler decreases the
290 amount of geopolymer matrix in the beads, lowering the specific surface area values for GAHT40-H
291 and GAHT60-H at around 14 $m^2 g^{-1}$. HTA-H beads have the lowest SSA (2 $m^2 g^{-1}$), since, as observed
292 before (Fig. 3l,m), the microstructure is formed by hydrotalcite particles covered and occluded by the
293 crosslinked alginate chains; in addition, the large shrinkage reduces the open porosity.
294 Freeze-dried -L beads, as a whole, show almost the same SSA values, comprised between 11 and 14
295 $m^2 g^{-1}$. Compared to the -H beads, - L beads show lower SSA values because in this process, water,
296 that is the geopolymerization reaction medium, is frozen, limiting to some extent the completion of
297 the reaction and the formation of the nanostructured matrix with its typical mesopores (Papa et al.,
298 2015). A similar SSA value, of 16 $m^2 g^{-1}$, was reported by Ge et al. 2017 for freeze-dried beads
299 obtained by ionotropic gelation of a slurry based on metakaolin, Na-silicate and Na-alginate solution.
300 HTA-L beads show an increase of SSA, because freeze-drying allowed to increase the porosity of the
301 beads, avoiding the excessive shrinkage obtained for HTA-H beads.
302
303 **3.3 Mechanical test**
304 The compressive strength was measured through the compaction of a bed of beads, following the ISO
305 18591 standard. In this way, a large number of beads was simultaneously measured, providing a more
306 accurate statistical value than that obtained from compression on a single bead.

307 The behavior of the beads during compression includes 3 main steps represented in Fig. 7 for beads
308 GA-H, taken as an example for the method used for compressive strength measurement.
309 The figure reports the logarithmic pressure curve in function of the relative density, and the average
310 compressive strength is measured by locating the spot where the curves have the steepest curvature.
311 Firstly, the beads pack and rearrange themselves in the die, increasing the relative density. In the 2$^{nd}$
312 step the compressive strength of the beads is exceeded and they start to fracture; here the pressure
313 changes in relation to density change. In the 3$^{rd}$ step the fractured beads rearrange till the load is
314 removed and the relief of pressure causes the release of elastic deformation (Järveläinen et al., 2016).
315 The average compressive strength of the bed is calculated using a constant compression speed, at the
316 point where the relative density increases most rapidly while the pressure increase is the slightest,
317 thus identifying the point of fracture. The spot is identified from the curve by extrapolating the linear
318 regressions from compression stages 1 and 3 and finding their intercept. To reduce experimental
319 noise, the first linear regression line was anchored to the relative density at 0.2 MPa. The second was
320 anchored to the relative density at the maximum pressure (Järveläinen et al., 2016).
321 The average compressive strength values and the critical densities for the different beads are reported
322 in Table 4. In general, the mix of alginate with the geopolymer matrix allows to overcome the
323 brittleness and the poor mechanical strength of pure crosslinked alginate beads.
324 GA-H beads have the highest compressive strength value equal to 9.2 MPa (Table 4), due to the good
325 combination between the geopolymerization process and the alginate crosslinking. The composite
326 beads GAHT40-H and GAHT60-H lower the value to about 6.0 MPa, probably because, respect to
327 the pure geopolymer matrix, the hydrotalcite powder acts as a defect, lowering the bound and creating
328 a bead with a less dense core. HTA-H beads lack of geopolymerization reaction and are formed by
329 hydrotalcite particles glued together by the crosslinked alginate skeleton. The good mechanical
330 resistance (6.5 MPa) is due to the formation of denser and harder spheres after the shrinkage occurred
331 during consolidation, probably because the high homogeneity of the beads led to a higher compaction
332 into the die (tapped density 0.8 g cm$^{-3}$, Table 3).

As expected, the freeze-dried beads show lower mechanical resistance: -L beads are more porous, expanded and with a spongy structure. GA-L, GAHT40-L and GAHT60-L beads have values comparable in the error limit (Table 4), while HTA-L beads present the lowest compressive strength value of 2.2 MPa. HTA-L beads have the highest open porosity (Table 3) with prevalence of macropores that decrease the mechanical resistance.

## 4. Conclusions

The results demonstrate that geopolymer-hydrotalcite hybrid beads can be produced by ionotropic gelation. Millimetre-sized, reproducible, uniform and spherical beads were obtained by dispersing a metakaolin-based geopolymer matrix and hydrotalcite particles into an alginate biopolymeric suspension, followed by crosslinking with calcium divalent ions. The beads were then subjected to consolidation in a heater at 60°C or freeze-dried.

The consolidation in the heater involves a greater dimensional shrinkage of the beads; consequently, the beads are dimensionally smaller with a rough external surface mainly formed by the Ca-alginate skeleton fold and stack in a worm-like configuration. The freeze-drying process allows to first freeze the water contained in the beads, which is subsequently sublimated, avoiding the shrinkage of the beads due to water evaporation, therefore the beads are slightly bigger with an external surface which is compact, smooth and dense. The internal microstructure is more porous, formed by wire-like Ca-alginate and granular geopolymer matrix forming a “honeycomb network”. The main difference between consolidation process regards the porosity, indeed the freeze-drying process allows to obtain beads with a higher open porosity, around 70%. The presence of different level of porosity could allow the rapid passage and diffusion of ionic species into the internal pores for contact with the different adsorptive sites present on the components of the beads.

Despite the different porosity, the composite beads obtained with the two consolidation methods show similar compressive strength values around 6 MPa, making them easy to handle and resistant in recovery, separation and filtration operations of aqueous systems.

Therefore, the consolidation processes produced beads different in terms of dimensions, morphology and porosity, potentially useful for the removal of different pollutants. In fact, the geopolymer matrix is an adsorbent for cationic species and at the same time is useful to shape and support the hydrotalcite filler, added in view of its potential adsorption of anionic species. Both hydrotalcite and alginate have good adsorption capacity but show deficiencies related to shaping, stability and mechanical strength, that are overcome in this case thanks to the presence of the geopolymer matrix.

This process strategy can be expanded to the entrapment of other micro-sized adsorbents in porous beads for a possible broad range of industrial applications in water purification and wastewater treatment.

**Acknowledgement**

The authors greatly thank Mr. Cesare Melandri for mechanical tests and Mr. Stefano Bassi for samples preparation.

**References:**

Asim, N., Alghoul, M., Mohammad, M., Amin, M.H., Akhtaruzzaman, M., Amin, N., Sopian, K., 2019. Emerging sustainable solutions for depollution: Geopolymers. Constr Build Mater. 199, 540-548. https://doi.org/10.1016/j.conbuildmat.2018.12.043

Bortnovsky, O., Dedecek, J., Tvaruzkova, Z., Sobalík, Z., Subrt, J., 2008. Metal ions as probes for characterization of geopolymer materials. J. Am. Ceram. Soc. 91, 3052-3057. https://doi.org/10.1111/j.1551-2916.2008.02577.x

Cavani, F., Trifirò, F., Vaccari, A., 1991. Hydrotalcite-type anionic clays: preparation, properties and applications. Catal. Today 11, 173-301. https://doi.org/10.1016/0920-5861(91)80068-K

Chen, F., Wang, K., Shao, L., Muhammad, Y., Wei, Y., Gao, F., Wang, X., Cui, X., 2019. Synthesis of $Fe_2O_3$-modified porous geopolymer microspheres for highly selective adsorption and

384 solidification of F- from waste-water. Composites Part B 178, 107497.
385 https://doi.org/10.1016/j.compositesb.2019.107497
386 Constantino, L.V., Quirino, J.N., Monteiro, A.M., Abrão, T., Parreira, P.S., Urbano, A., Santos,
387 M.J., 2017. Sorption-desorption of selenite and selenate on Mg-Al layered double hydroxide in
388 competition with nitrate, sulphate and phosphate. Chemosphere 181, 627-634.
389 https://doi.org/10.1016/j.chemosphere.2017.04.071
390 Crini, G., Lichtfouse, E., Wilson, L. D., Morin-Crini, N., 2019. Conventional and non-conventional
391 adsorbents for wastewater treatment. Environ. Chem. Lett. 17, 195–213.
392 https://doi.org/10.1007/s10311-018-0786-8
393 Davidovits, J., 2008. Geopolymers Chemistry and Applications, Institut Geopolymere: Saint-
394 Quentin, France.
395 Ge, Y., Cui, X., Kong, Y., Li, Z., He, Y., Zhou, Q., 2015. Porous geopolymeric spheres for removal
396 of Cu(II) from aqueous solution: synthesis and evaluation. J. Hazard. Mater. 283, 244-251.
397 https://doi.org/10.1016/j.jhazmat.2014.09.038
398 Ge, Y., Cui, X., Liao, C., Li, Z., 2017. Facile fabrication of green geopolymer/alginate hybrid
399 spheres for efficient removal of Cu(II) in water: batch and column studies. Chem. Eng. J. 311, 126-
400 134. https://doi.org/10.1016/j.cej.2016.11.079
401 Goh, K.-H., Lim, T.-T., Dong, Z., 2008. Application of layered double hydroxides for removal of
402 oxyanions: a review. Water Res. 42, 1343-1368. https://doi.org/10.1016/j.watres.2007.10.043
403 Järveläinen, M., Kaleva, A., Kaitajärvi, A., Laakso, J., Kanerva, U., Levänen, E., 2016.
404 Compression curve analysis and compressive strength measurement of brittle granule beds in lieu of
405 individual granule measurements. Particuology 29, 60–68.
406 https://doi.org/10.1016/j.partic.2015.10.006
407 Ji, H., Wu, W., Li, F., Yu, X., Fu, J., Jia, L., 2017. Enhanced adsorption of bromate from aqueous
408 solutions on ordered mesoporous Mg-Al layered double hydroxides (LDHs). J. Hazard. Mater. 334,
409 212-222. https://doi.org/10.1016/j.jhazmat.2017.04.014

Kumar, I.A., Viswanathan, N., 2017. Fabrication of metal ions cross-linked alginate assisted biocomposite beads for selective phosphate removal. J. Environ. Chem. Eng. 5, 1438–1446. https://doi.org/10.1016/j.jece.2017.02.005

Leong, J-Y., Lam, W-H., Ho, K-W., Voo, W-P., Lee, M. F-X., Lim, H-P., Lim, S-L., Tey, B-T., Poncelet, D., Chan, E-S., 2016. Advances in fabricating spherical alginate hydrogels with controlled particle designs by ionotropic gelation as encapsulation systems. Particuology 24, 44–60. https://doi.org/10.1016/j.partic.2015.09.004

Liu, Z.-H., Tang, Q., Li, C.-M., He, Y., Cui, X.-M., 2017. Preparation of NaA zeolite spheres from geopolymer gels using a one-step method in silicone oil. Int. J. Appl. Ceram. Technol. 14, 982-986. https://doi.org/10.1111/ijac.12708

Luukkonen, T., Heponiemi, A., Runtti, H., Pesonen, J., Yliniemi, J., Lassi, U., 2019. Application of alkali-activated materials for water and wastewater treatment: a review. Rev. Environ, Sci. Biotechnol. 18, 271-297. https://doi.org/10.1007/s11157-019-09494-0

Luukkonen, T., Sarkkinen, M., Kemppainen, K., Rämö, J., Lassi, U., 2016. Metakaolin geopolymer characterization and application for ammonium removal from model solutions and landfill leachate. App. Clay Sci. 119, 266-276. https://doi.org/10.1016/j.clay.2015.10.027

Mandal, S., Patil, V.S., Mayadevi, S., 2012. Alginate and hydrotalcite-like anionic clay composite systems: Synthesis, characterization and application studies. Microporous Mesoporous Mater. 158, 241–246. https://doi.org/10.1016/j.micromeso.2012.03.046

Mandal, S., Mayadevi, S., 2008. Cellulose supported layered double hydroxides for the adsorption of fluoride from aqueous solution, Chemosphere 72, 995–998. https://doi.org/10.1016/j.chemosphere.2008.03.053

Medri, V., Papa, E., Dedecek, J., Jirlova, H., Benito, P., Vaccari, A., Landi, E., 2013. Effect of metallic Si addition on polymerization degree of in situ foamed alkali-aluminosilicates. Ceram. Int. 39, 7657-7668. https://doi.org/10.1016/j.ceramint.2013.02.104

435 Medri, V., Papa, E., Lizion, J. Landi, E., 2020a. Metakaolin-based geopolymer beads: Production
436 methods and characterization. J. Clean. Prod. 244, 118844.
437 https://doi.org/10.1016/j.jclepro.2019.118844
438 Medri, V., Papa, E., Mor, M., Vaccari, A., Natali Murri, A., Piotte, L., Melandri, C., Landi, E., 2020b.
439 Mechanical strength and cationic dye adsorption ability of metakaolin-based geopolymer spheres.
440 App. Clay Sci. 193, 105678. https://doi.org/10.1016/j.clay.2020.105678
441 Novais, R.M., Seabra, M.P., Labrincha J.A., 2017. Porous geopolymer spheres as novel pH buffering
442 materials. J. Clean. Prod. 143, 1114-1122. https://doi.org/10.1016/j.jclepro.2016.12.008
443 Pan, B., Pan, B., Zhang, W., Lv, L., Zhang, Q., Zheng, S., 2009. Development of polymeric and
444 polymer-based hybrid adsorbents for pollutants removal from waters. Chem. Eng. J. 151, 19-29.
445 https://doi.org/10.1016/j.cej.2009.02.036
446 Papa, E., Medri, Benito, P., Vaccari, A., Bugani, S., Jaroszewicz, J., Swieszkowski, W., Landi, E.,
447 2015. Synthesis of porous hierarchical geopolymer monoliths by ice-templating. Microporous
448 Mesoporous Mater. 215, 206-214. https://doi.org/10.1016/j.micromeso.2015.05.043
449 Papa, E., Medri, V., Amari, S., Manaud, J., Benito, P., Vaccari, A., Landi, E., 2018. Zeolite-
450 geopolymer composite materials: production and characterization. J. Clean. Prod. 171, 76-84.
451 https://doi.org/10.1016/j.jclepro.2017.09.270
452 Papa, E., Medri, Paillard, C., Contri, B., Natali Murri, A., Vaccari, A., Landi, E., 2019.Geopolymer-
453 hydrotalcite composites for $CO_2$ capture. J. Clean. Prod. 237, 117738.
454 https://doi.org/10.1016/j.jclepro.2019.117738
455 Papa, E., Mor, M., Natali Murri, A., Landi, E., Medri, V., 2020. Ice-templated geopolymer beads for
456 dye removal, J. Colloid. Interf. Sci. 15 (2020) 364-373. https://doi.org/10.1016/j.jcis.2020.03.104
457 Rasaki, S.A., Bingxue, Z., Guarecuco, R., Thomas, T., Minghui, Y., 2019. Geopolymer for use in
458 heavy metals adsorption, and advanced oxidative processes: A critical review. J. Clean. Prod. 213,
459 42-58. https://doi.org/10.1016/j.jclepro.2018.12.145

Runtti, H., Luukkonen, T., Niskanen, M., Tuomikoski, S., Kangas, T., Tynjälä, P., Tolonen, E-T., Sarkkinen, M., Kemppainen, K., Rämö, J., Lassi, U., 2016. Sulphate removal over barium-modified blast-furnace-slag geopolymer. J. Hazard. Mater. 317, 373–384. https://doi.org/10.1016/j.jhazmat.2016.06.001

Siyala, A.A., Shamsuddina, M.R., Khana, M.I., Rabata, N.E., Zulfiqara, M., Mana, Z., Siamec, J., Azizli, K.A., 2018. A review on geopolymers as emerging materials for the adsorption of heavy metals and dyes. J. Environ. Manage. 224, 327–339. https://doi.org/10.1016/j.jenvman.2018.07.046

Tan, T. H., Moa, K. H., Ling, T-C, Lai, S. H., 2020. Current development of geopolymer as alternative adsorbent for heavy metal removal. Environ. Technol. Innov. 18, 100684. https://doi.org/10.1016/j.eti.2020.100684

Tang, Q., Ge, Y.-Y., Wang, K.-T., He, Y., Cui, X.-M., 2015. Preparation and characterization of porous metakaolin-based inorganic polymer spheres as an adsorbent. Mater. Des. 88, 1244-1249. https://doi.org/10.1016/j.matdes.2015.09.126

Tang, Q., Xue, G.-H., Yang, S.-J., Wang, K., Cui, X.-M., 2017. Study on the preparation of a free-sintered inorganic polymer-based proppant using the suspensions solidification method. J. Clean. Prod. 148, 276-282. https://doi.org/10.1016/j.jclepro.2017.02.001

Tian, Q., Guo, B., Sasaki, K., 2020. Immobilization mechanism of Se oxyanions in geopolymer: Effects of alkaline activators and calcined hydrotalcite additive. J. Hazard. Mater. 387, 121994. https://doi.org/10.1016/j.jhazmat.2019.121994

Tian, Q., Sasaki, K., 2019. Novel composite of layered double hydroxide/geopolymer for co-immobilization of $Cs^{+}$ and $SeO_4^{2-}$ from aqueous solution. Sci Total Environ 695, 133799. https://doi.org/10.1016/j.scitotenv.2019.133799

Vaccari, A., 1998. Preparation and catalytic properties of cationic and anionic clays. Catal. Today 41, 53-71. https://doi.org/10.1016/S0920-5861(98)00038-8

Voo, W-P., Ooi, C-W., Islam, A., Tey, B-T., Chan, E-S., 2016. Calcium alginate hydrogel beads with high stiffness and extended dissolution behaviour. Eur. Polym. J. 75 (2016) 343–353. https://doi.org/10.1016/j.eurpolymj.2015.12.029

Wang, K., Lei, H., Muhammad, Y., Chen, F., Gao, F., Wei, Y., Fujita, T., 2020. Controlled preparation of cerium oxide loaded slag-based geopolymer microspheres (CeO2@SGMs) for the adsorptive removal and solidification of F− from acidic waste-water. J. Hazard. Mater. 400, 123199. https://doi.org/10.1016/j.jhazmat.2020.123199

Graphical Abstract

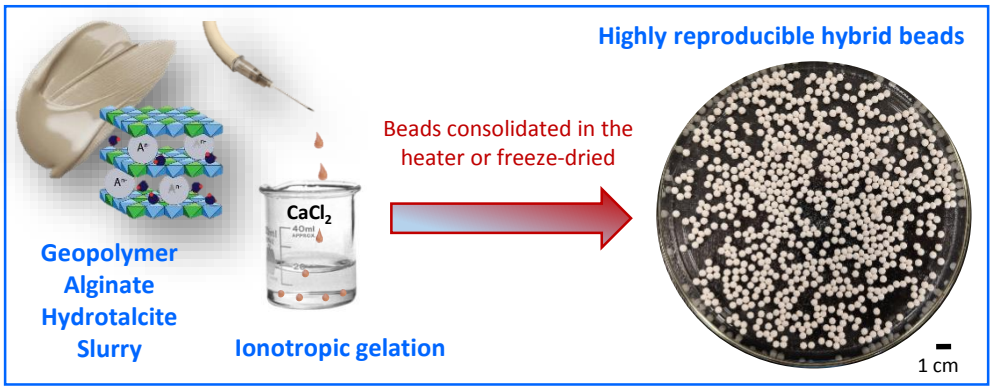

Highlights

- Geopolymer-hydrotalcite hybrid beads were produced by ionotropic gelation
- Beads were finally consolidated in a heater or by a freeze-drying process
- Highly reproducible beads with different morphology and porosity were obtained
- Beads were easy to handle and resistant, with a compressive strength around 6 MPa
- Composite beads are potentially useful for the removal of different pollutants

**Table 1.** Beads codes, mixing ratio for the formulation of the slurries, weight percent of hydrotalcite present in the final consolidated beads and consolidation method adopted.

| Beads Code | Mixing ratio (wt.%) | | | HT in the final beads (wt.%) | Consolidation method |
|---|---|---|---|---|---|
| | Geopolymer slurry | Na Alginate solution | HT | | |
| GA-H | 18 | 82 | - | - | Heater |
| GAHT40-H | 17 | 78 | 5 | 40 | Heater |
| GAHT60-H | 17 | 76 | 7 | 60 | Heater |
| HTA-H | - | 86 | 14 | 100 | Heater |
| GA-L | 18 | 82 | - | - | Freeze-drying |
| GAHT40-L | 17 | 78 | 5 | 40 | Freeze-drying |
| GAHT60-L | 17 | 76 | 7 | 60 | Freeze-drying |
| HTA-L | - | 86 | 14 | 100 | Freeze-drying |

**Table 2.** Average major diameter and roundness calculated by image analysis on 300 beads for each batch type and diameter shrinkage after consolidation.

| Sample | Major Ø (mm) | Roundness | Major Ø shrinkage (%) |
|---|---|---|---|
| GA fresh | 4.12 ± 0.14 | 0.88 ± 0.06 | |
| GA-H | 2.70 ± 0.08 | 0.90 ± 0.08 | -35 |
| GA-L | 3.50 ± 0.21 | 0.90 ± 0.06 | -15 |
| GAHT40 fresh | 4.06 ± 0.17 | 0.89 ± 0.06 | |
| GAHT40-H | 3.00 ± 0.09 | 0.92 ± 0.07 | -26 |
| GAHT40-L | 3.63 ± 0.22 | 0.90 ± 0.07 | -11 |
| GAHT60 fresh | 4.18 ± 0.12 | 0.89 ± 0.05 | |
| GAHT60-H | 3.11 ± 0.12 | 0.91 ± 0.06 | -26 |
| GAHT60-L | 3.45 ± 0.16 | 0.90 ± 0.06 | -18 |
| HTA fresh | 3.91 ± 0.14 | 0.91 ± 0.04 | |
| HTA-H | 2.35 ± 0.13 | 0.91 ± 0.06 | -40 |
| HTA-L | 3.78 ± 0.21 | 0.90 ± 0.05 | -3 |

**Table 3.** Tapped density, porosity data obtained by MIP and BET specific surface area (SSA).

| Sample | Tapped density (g $cm^{-3}$) | Open porosity (%) | Total pore volume ($mm^3$ $g^{-1}$) | Average pore Ø (µm) | Modal pore Ø (µm) | SSA ($m^2$ $g^{-1}$) |
|---|---|---|---|---|---|---|
| GA-H | 0.5 | 50 | 562 | 0.09 | 0.15 | 23 |
| HTA-H | 0.8 | 20 | 131 | 0.02 | 0.01 | 2 |
| GAHT40-H | 0.5 | 54 | 634 | 0.11 | 0.28 | 14 |
| GAHT60-H | 0.5 | 53 | 639 | 0.11 | 0.33 | 15 |
| | | | | | | |
| GA-L | 0.4 | 68 | 1144 | 0.16 | 0.16 | 14 |
| HTA-L | 0.2 | 73 | 1584 | 0.27 | 25.10 | 11 |
| GAHT40-L | 0.4 | 60 | 993 | 0.15 | 0.34 | 12 |
| GAHT60-L | 0.4 | 70 | 1147 | 0.17 | 0.30 | 13 |

**Table 4.** Compressive strength Pc and critical density ρc with standard deviation values, of the different beads obtained according to ISO / 18591.

| Beads Code | Pc (MPa) | ρc (g $cm^{-3}$) |
|---|---|---|
| GA-H | 9.2 ± 0.7 | 0.67 ± 0.01 |
| GAHT40-H | 5.8 ± 0.7 | 0.63 ± 0.05 |
| GAHT60-H | 5.9 ± 0.5 | 0.65 ± 0.02 |
| HTA-H | 6.5 ± 0.4 | 0.92 ± 0.02 |
| GA-L | 6.0 ± 0.5 | 0.56 ± 0.01 |
| GAHT40-L | 5.8 ± 0.4 | 0.64 ± 0.02 |
| GAHT60-L | 6.5 ± 1.3 | 0.68 ± 0.05 |
| HTA-L | 2.2 ± 0.7 | 0.47 ± 0.22 |

**Figure captions**

**Figure 1.** Schematic diagram of the production process of the beads.

**Figure 2.** Major diameter distributions for «fresh» shaped beads and after consolidation (heater - H, and freeze-drying, -L). Beads obtained from slurries: GA (a), HTA (b), GAHT40 (c), GAHT60 (d).

**Figure 3.** SEM micrographs of beads GA-H (a,b,c), GAHT40-H (d,e,f), GAHT60-H (g,h,i) and HTA-H (l,m,n), obtained after consolidation in the heater. Whole beads (a,d,g,l), external (b,e,h,m) and internal (c,f,i,n) surfaces.

**Figure 4.** SEM micrographs of beads GA-L (a,b,c), GAHT40-L (d,e,f), GAHT60-L (g,h,i) and HTA-L (l,m,n), obtained after consolidation in the freeze-dryer. Whole beads (a,d), cross sections (g,l), external (b,e,h,m) and internal (c,f,i,n) surfaces.

**Figure 5.** Pore size distributions by MIP of GA-H (a), HTA-H (b), GAHT40-H (c) and GAHT60-H (d) beads.

**Figure 6.** Pore size distributions by MIP of GA-L (a), HTA-L (b), GAHT40-L (c) and GAHT60-L (d) beads.

**Figure 7.** Illustration of a compressive curve, for GA-H beads, showing the 3 steps that occurred during the compression and step 1 and step 3 asymptotes (dashed lines) used to calculate the average compressive strength (arrow).

Figure 1

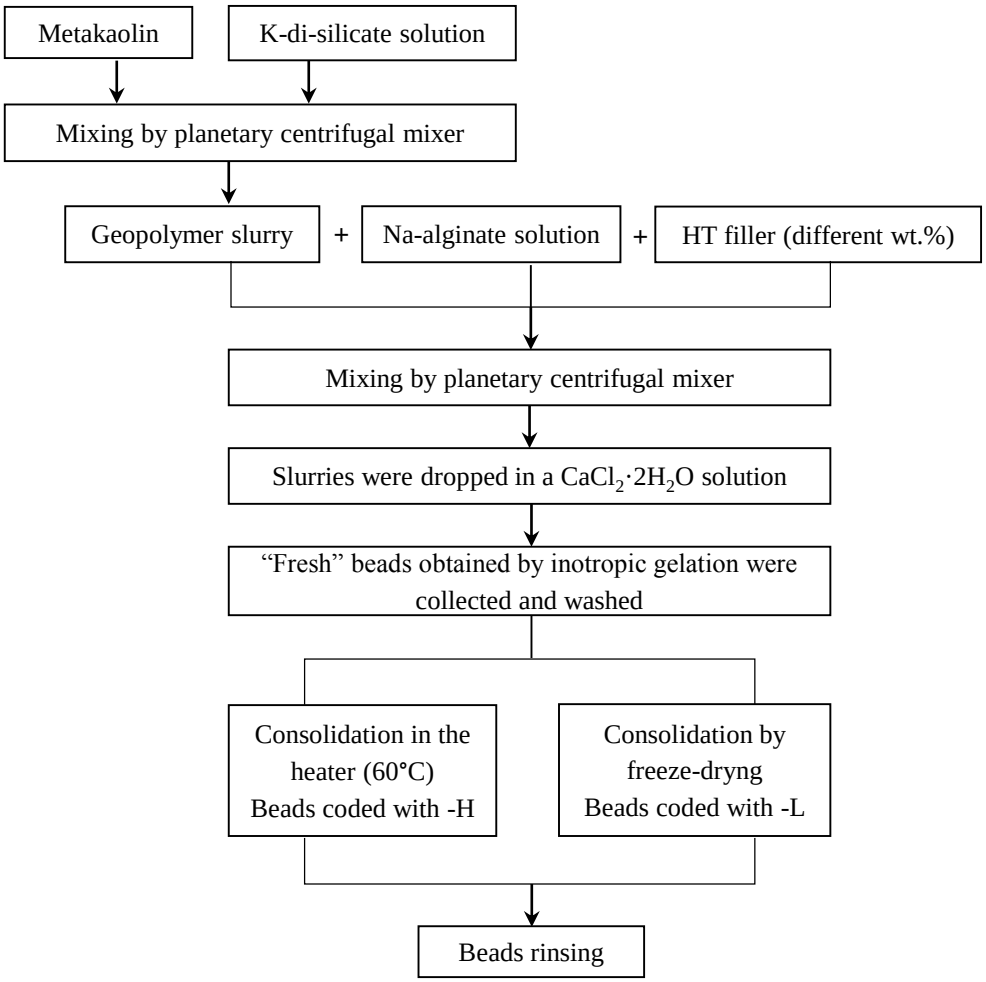
Metakaolin
K-di-silicate solution
Mixing by planetary centrifugal mixer
Geopolymer slurry
+
Na-alginate solution
+
HT filler (different wt.%)
Mixing by planetary centrifugal mixer
Slurries were dropped in a $CaCl_2 \cdot 2H_2O$ solution
"Fresh" beads obtained by inotropic gelation were collected and washed
Consolidation in the heater (60°C) Beads coded with -H
Consolidation by freeze-dryng Beads coded with -L
Beads rinsing

Figure 2

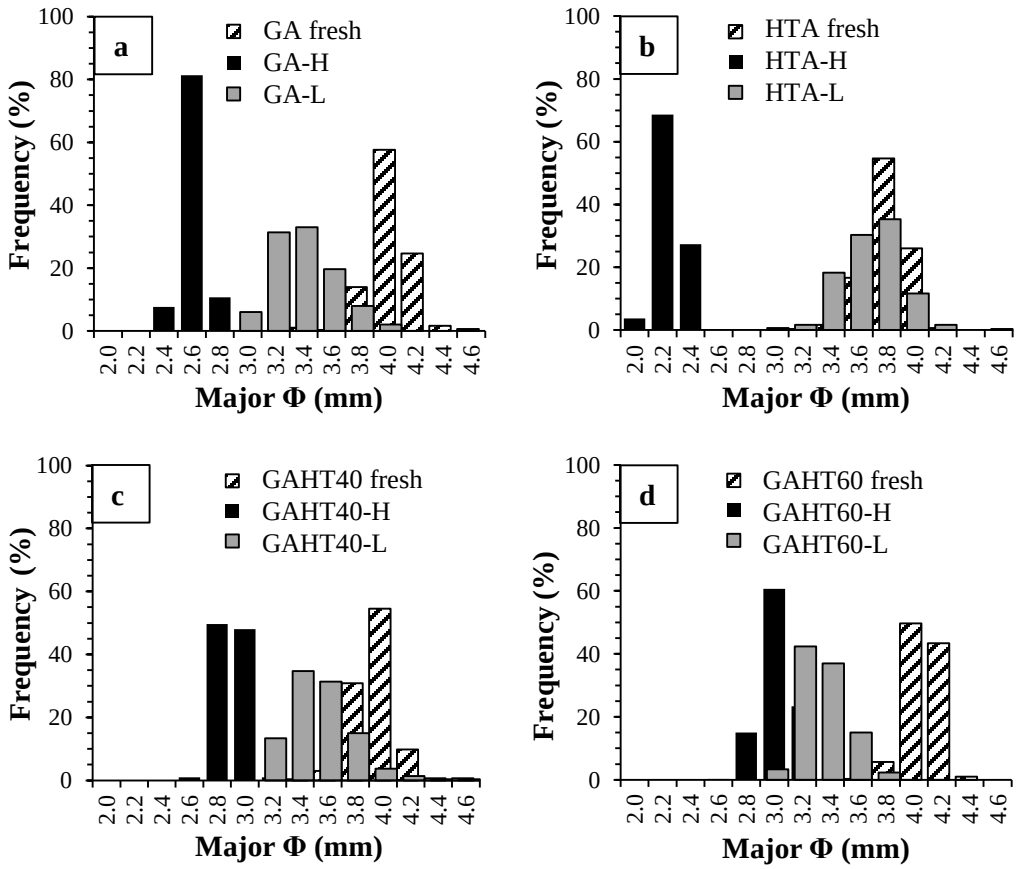
a
GA fresh
GA-H
GA-L
b
HTA fresh
HTA-H
HTA-L
c
GAHT40 fresh
GAHT40-H
GAHT40-L
d
GAHT60 fresh
GAHT60-H
GAHT60-L
Frequency (%)
Major Φ (mm)
0
20
40
60
80
100
2.0
2.2
2.4
2.6
2.8
3.0
3.2
3.4
3.6
3.8
4.0
4.2
4.4
4.6

Figure 3

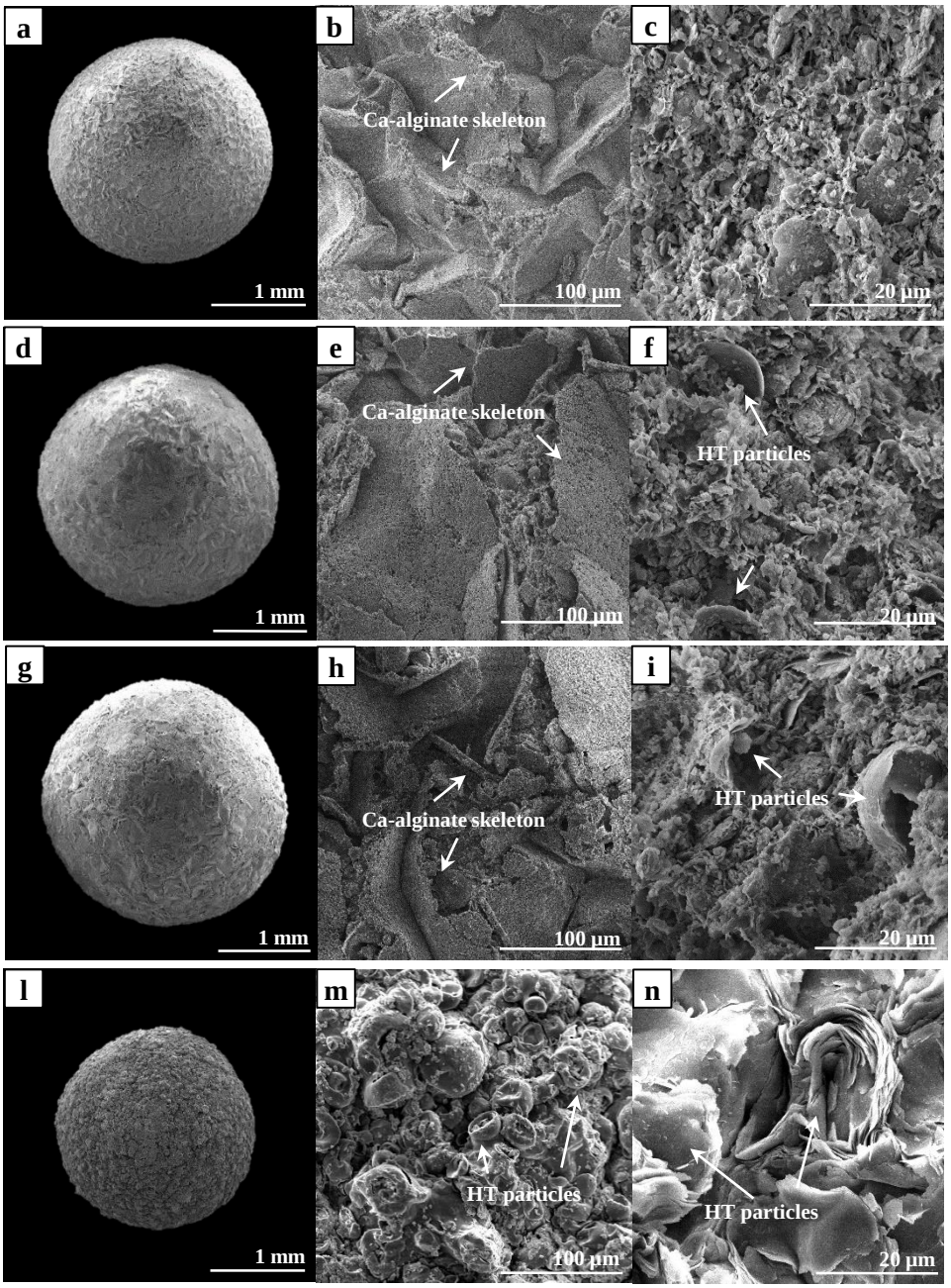
a
1 mm
b
Ca-alginate skeleton
100 µm
c
20 µm
d
1 mm
e
Ca-alginate skeleton
100 µm
f
HT particles
20 µm
g
1 mm
h
Ca-alginate skeleton
100 µm
i
HT particles
20 µm
l
1 mm
m
HT particles
100 µm
n
HT particles
20 µm

Figure 4

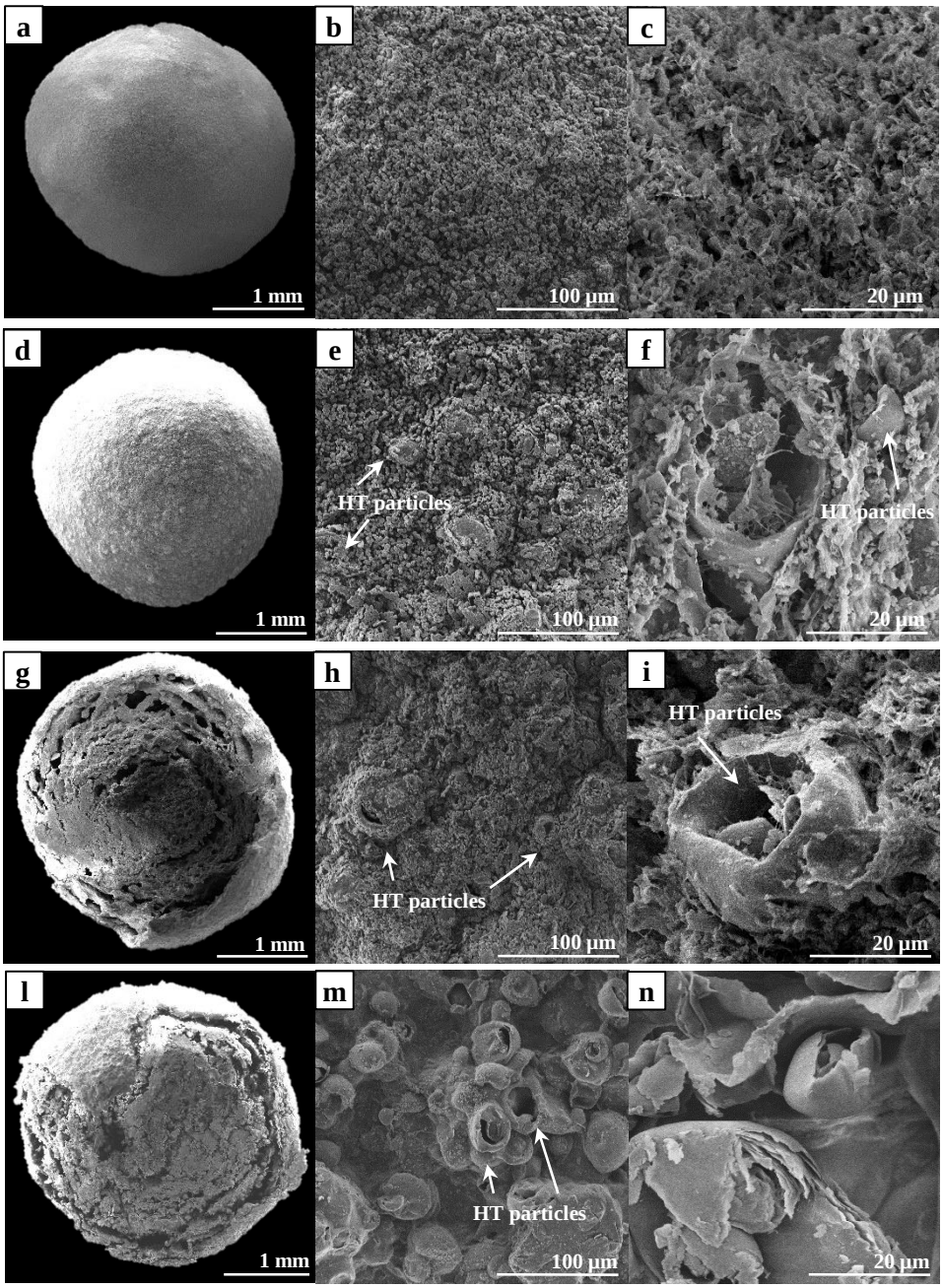
a
1 mm
b
100 µm
c
20 µm
d
1 mm
e
HT particles
100 µm
f
HT particles
20 µm
g
1 mm
h
HT particles
100 µm
i
HT particles
20 µm
l
1 mm
m
HT particles
100 µm
n
20 µm

Figure 5

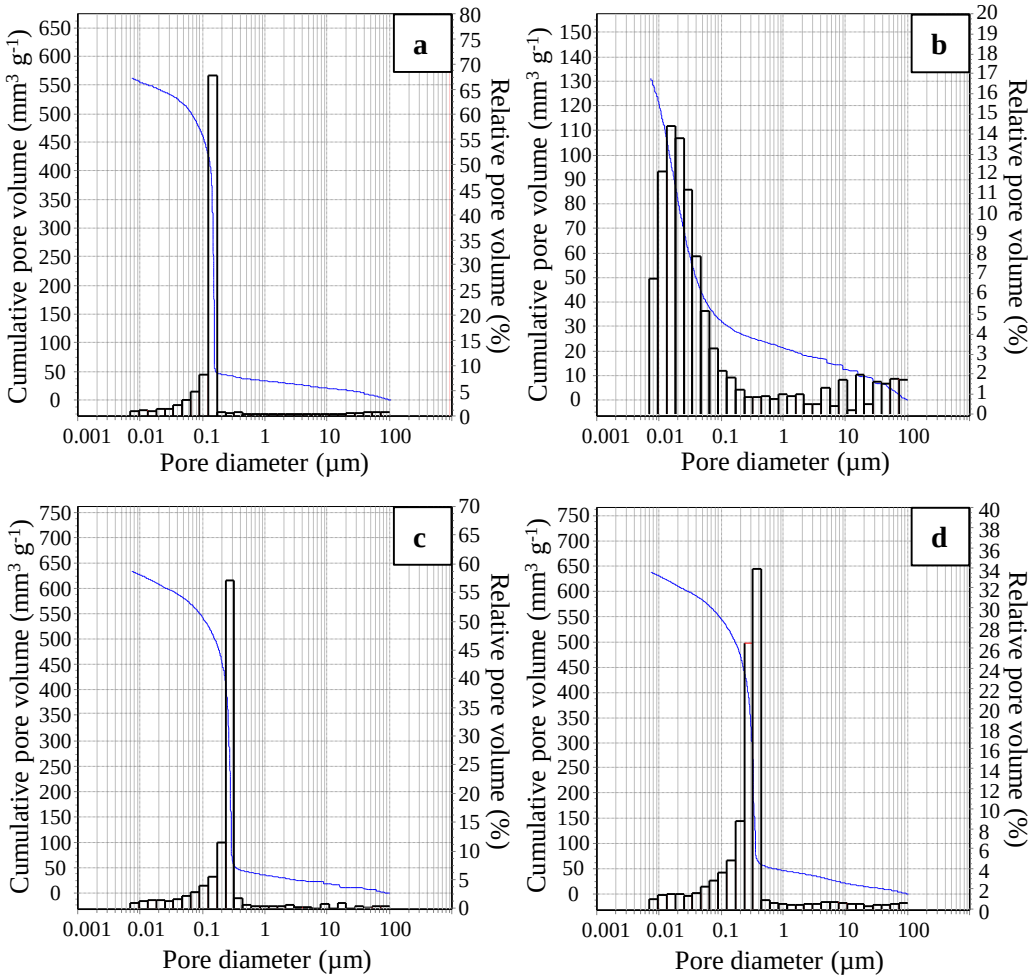
a
b
c
d
Cumulative pore volume (mm3 g-1)
Relative pore volume (%)
Pore diameter (µm)
0.001
0.01
0.1
1
10
100

Figure 6

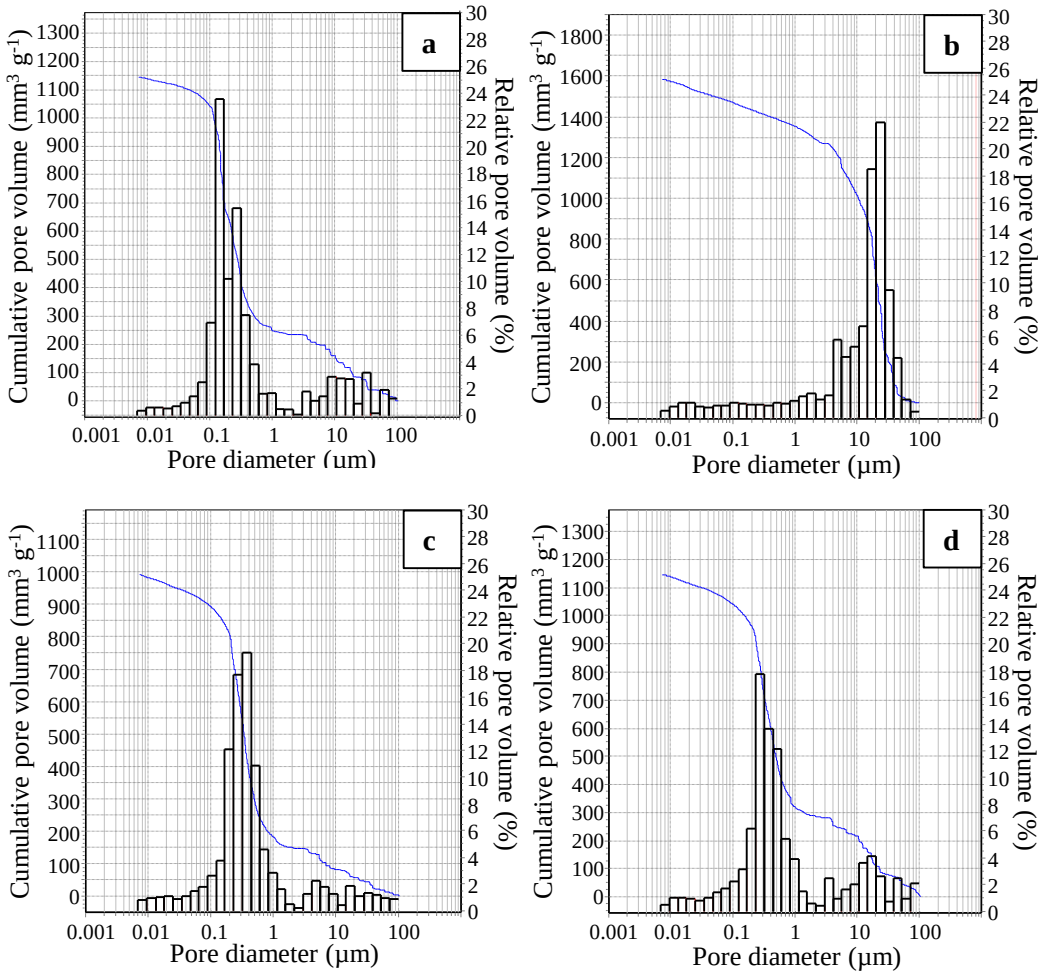
a
b
c
d
Cumulative pore volume (mm3 g-1)
Relative pore volume (%)
Pore diameter (µm)
0.001
0.01
0.1
1
10
100

Figure 7

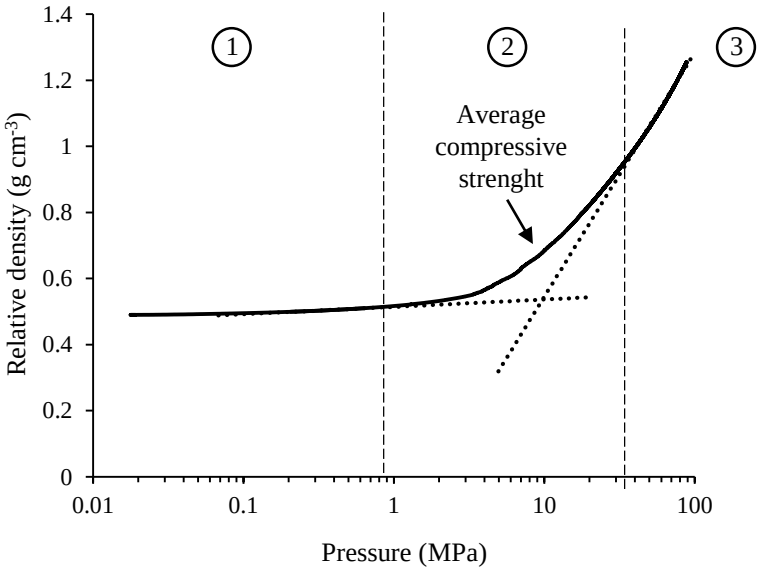
1
2
3
Average
compressive
strenght
Relative density (g cm-3)
1.4
1.2
1
0.8
0.6
0.4
0.2
0
0.01
0.1
1
10
100
Pressure (MPa)

**Author statement**

**Elettra Papa:** Data curation, Investigation, Writing- Original draft preparation. **Annalisa Natali Murri:** Visualization, Writing- Reviewing and Editing. **Angelo Vaccari:** Conceptualization, Resources. **Elena Landi:** Methodology, Supervision. **Valentina Medri:** Conceptualization, Writing- Reviewing and Editing, Supervision, Resources